Atmos. Chem. Phys. Discuss., 10, 22515–22552, 2010
www.atmos-chem-phys-discuss.net/10/22515/2010/
doi:10.5194/acpd-10-22515-2010

Atmospheric Chemistry and Physics Discussions

Technical Note: Cloud and aerosol effects on rotational Raman scattering: measurement comparisons and sensitivity studies

A. Kylling[1], **B. Mayer**[2], **and M. Blumthaler**[3]

[1]AFKIRL Consultant, Ålesund, Norway
[2]Meteorological Institute, Ludwig-Maximilians-University, Munich, Germany
[3]Division for Biomedical Physics, Innsbruck Medical University, Innsbruck, Austria

Received: 10 August 2010 – Accepted: 6 September 2010 – Published: 1 October 2010

Correspondence to: A. Kylling (arve.kylling@gmail.com)

Published by Copernicus Publications on behalf of the European Geosciences Union.

Abstract

Rotational Raman scattering in the Earth's atmosphere explains the filling-in of Fraunhofer lines in the solar spectrum. Based on the versatile DISORT (Stamnes et al., 1988) radiative transfer solver, a new model including single rotational Raman scattering, has been developed and implemented into the freely available libRadtran radiative transfer package (Mayer and Kylling, 2005). The model is successfully compared against measurements of the differential optical depth for both optically thick clouds and aerosol loaded cases. Subsequently, the model is used for various sensitivity studies to investigate how clouds and aerosol affect the filling-in of the calcium K line.

1 Introduction

Most of the UV, visible and infrared photons scattered in the Earth's atmosphere are elastically scattered, that is, they do not change wavelength during the scattering process. However, a fraction of the photons are inelastically scattered by air, dominantly nitrogen and oxygen, molecules. This inelastic scattering process is attributed to rotational Raman scattering, (Kattawar et al., 1981). Rotational Raman scattering in the Earth's atmosphere explains the so-called filling-in of Fraunhofer lines in solar spectra measured both from the Earth's surface and onboard satellites. Rotational Raman scattering is of importance because it affects the accuracy of trace gase retrievals. Furthermore, the rotational Raman scattering signal may be used to estimate cloud top pressure from satellite measurements and aerosol properties from both surface and satellite observations.

Numerous numerical models exist for the treatment of elastic multiple scattering of photons in the Earth's atmosphere. The inclusion of inelastic scattering is more demanding and typically rotational Raman scattering is treated as a perturbation with only first-order rotational Raman scattering being accounted for. Several authors have developed radiative transfer models that account for rotational Raman scattering,

ACPD
10, 22515–22552, 2010

including Joiner et al. (1995); Vountas et al. (1998); Landgraf et al. (2004); van Deelen et al. (2007); Spurr et al. (2008); Wagner et al. (2009a).

The model of Joiner et al. (1995) is a scalar successive order of scattering code including single rotational Raman scattering. Successive order of scattering codes are generally not well suited for explicit treatment of clouds. Vountas et al. (1998) described a first order rotational Raman scattering model that treated clouds explicitly. This model was used by de Beek et al. (2001) to study the effect of rotational Raman scattering on both ground-based and satellite measurements. Spurr et al. (2008) described a discrete ordinates method model for rotational Raman scattering and presented model simulations of filling-in factors due to single order rotational Raman scattering in cloudy situations. Both results for satellite geometries and vertical profiles of filling-in factors were shown. Wagner et al. (2009a) presented the first 3-D Monte Carlo simulations of first order rotational Raman scattering in the presence of horizontally inhomogeneous (cubical) clouds. This model has been used to determine aerosol properties from both surface multi-axis differential optical absorption spectroscopy (MAX-DOAS) observations of the ring effect (Wagner et al., 2009b) and satellite observations of the ring effect (Wagner et al., 2010).

All the above codes are scalar codes, that is, they do not include polarization. Landgraf et al. (2004) presented a vector radiative transfer model including single rotational Raman scattering. They found that the neglect of polarization on Raman scattering is of minor importance for most applications. It is noted however, that polarization itself may be of importance, see for example Emde et al. (2010) and references therein. van Deelen et al. (2007) developed a doubling-adding code including multiple elastic and multiple inelastic rotational Raman scattering. They found that the error of the single rotational Raman scattering approximation compared to the multiple scattering solution is subpercentage.

In this paper a new discrete ordinates radiative transfer model including single rotational Raman scattering is presented. The model is used to explain spectral structures in ground based irradiance measurements of the differential optical depth for

ACPD
10, 22515–22552, 2010

both optically thick clouds and aerosol loaded cases. Subsequently the model is used in sensitivity studies to estimate the effect of aerosol, cloud height, vertical cloud extension and cloud optical depth for both ground-based and satellite geometries on filling-in of Fraunhofer lines. The differing effects of rotational Raman scattering on radiances and irradiances are addressed.

The paper is organized as follows: first the radiative transfer model and the input for the thunderstorm and aerosol cases are presented. Secondly, the measurements for the thunderstorm and aerosol cases are described. This is followed by a comparison of model results and measurements for the two cases. A sensitivity study of some effects of clouds and aerosols are subsequently presented before the paper is concluded.

2 Radiative transfer model and atmospheric inputs

The radiative transfer equation including first order rotational Raman scattering, has been derived by for example Vountas et al. (1998) and Landgraf et al. (2004). For radiation at wavelength λ and location r, the radiative transfer equation including rotational Raman scattering may be written as (Vountas et al., 1998, Eq. 10)

$$\mathcal{R}I(r,\Omega,\lambda) = \varepsilon_{\mathrm{rrs}}(r,\Omega,\lambda), \tag{1}$$

where $\{\Omega\} = \{\mu,\phi\}$, μ is the cosine of the polar angle and ϕ is the azimuth angle. The integro-differential operator in a one dimensional atmosphere is

$$\mathcal{R} = \mu\frac{d}{dr} + \beta^{\mathrm{ext}}(r,\lambda) - \frac{\beta^{\mathrm{sca}}(r,\lambda)}{4\pi}\int d\Omega' P(r,\Omega,\Omega',\lambda). \tag{2}$$

Here $P(r,\Omega,\Omega',\lambda)$ is the phase function and $\beta^{\mathrm{ext}}=\beta^{\mathrm{abs}}+\beta^{\mathrm{sca}}$, $\beta^{\mathrm{abs}}(r,\lambda)=\sum_i \beta_i^{\mathrm{abs}}(r,\lambda)$, $\beta_i^{\mathrm{abs}}(r,\lambda)=n_i(r)\sigma_i^{\mathrm{abs}}(\lambda)$ and similar for the scattering coefficient (Stamnes, 1986). The vertical profile of specie i is denoted by $n_i(r)$, and $\sigma_i(\lambda)$ is the corresponding absorption

ACPD
10, 22515–22552, 2010

or scattering cross section. The summation over i for β^{sca} includes Rayleigh scattering, and scattering of aerosols and clouds. For the absorption coefficient it includes absorption by clouds, aerosols and various molecular species. Finally

$$\varepsilon_{\mathrm{rrs}}(r,\Omega,\lambda) =$$
$$\sum_{s=1}^{N} \frac{\beta_{\mathrm{rrs}}(r,\lambda_s,\lambda)}{4\pi} \int d\Omega' I(r,\Omega',\lambda_{\mathrm{s}}) P_{\mathrm{rrs}}(\Omega,\Omega',\lambda_{\mathrm{s}})$$
$$-\sum_{s=1}^{N} \frac{\beta_{\mathrm{rrs}}(r,\lambda,\lambda_{\mathrm{s}})}{4\pi} \int d\Omega' I(r,\Omega',\lambda) P_{\mathrm{rrs}}(\Omega,\Omega',\lambda), \quad (3)$$

where β_{rrs} is the rotational Raman scattering coefficient and the Raman phase function $P_{\mathrm{rrs}}(\Phi)=3/40(13+\cos^2\Phi)$. The first term on the right hand side of Eq. (3) represents photons that are Raman scattered from other wavelenghts λ_{s} into the wavelength λ of interest. Similarly, the second term represents photons that are Raman scattered out of the wavelength λ and into the Raman lines λ_{s}. Neglecting Raman scattering and setting $\varepsilon_{\mathrm{rrs}}(r,\Omega,\lambda)=0$, gives the standard 1D radiative transfer equation for elastic scattering. The technical details of the solution of Eq. (1) are briefly outlined in Appendix A.

The libRadtran radiative transfer software package (Mayer and Kylling, 2005) has been extended to account for single rotational Raman scattering. In this study the uvspec radiative transfer equation solver from libRadtran was used to calculate radiation spectra with and without rotational Raman scattering.

Two different experimental cases were considered. The first case involved a thunderstorm over Garmisch-Partenkirchen, Germany (Mayer et al., 1998). The second case from Nea Michinanona, Greece, utilizes measurements made under a heavy aerosol load (Kylling et al., 2003).

For the simulation of the measurements, high-resolution spectra with a step width of 0.05 nm were calculated. They were subsequently convolved with the instrument slit function and interpolated to the lower-resolution wavelength grid of the observations. To concentrate on Raman scattering and to avoid uncertainties caused by missing

ACPD
10, 22515–22552, 2010

knowledge of the ozone profile, the wavelength region 340–410 nm, where ozone absorption is negligible, was investigated. NO_2 was included as the only molecular absorber. It, however, has only little impact (less than a percent) in this wavelength region.

The so-called filling-in factor FI is often used to describe the magnitude of rotational Raman scattering. It involves the ratio of modelled radiation quantities with and without rotational Raman scattering. Several definitions of the filling-in factor are used in the literature (Joiner and Bhartia, 1995; de Beek et al., 2001; Langford et al., 2007; Spurr et al., 2008). Here, the definition of Spurr et al. (2008) is adopted,

$$\mathrm{FI}(\lambda) = 100\% \left(1 - \frac{E_{\mathrm{elastic}}(\lambda)}{E_{\mathrm{inelastic}}(\lambda)}\right), \quad (4)$$

where E_{elastic} and $E_{\mathrm{inelastic}}$ are the calculated irradiances without and with rotational Raman scattering, respectively. For the profiles the filling-in is calculated locally, that is, both E_{elastic} and $E_{\mathrm{inelastic}}$ are calculated at the same altitude.

To compare the model results with the measurements the differential optical depth, DOD, was calculated,

$$\mathrm{DOD} = \ln(E/E_{\mathrm{ref}}) - P. \quad (5)$$

Here, E_{ref} is the reference spectrum, E the spectrum of interest, and P a third degree polynomial that accounts for broadband features including Rayleigh scattering, aerosol absorption and scattering, and cloud scattering in the wavelength region under investigation.

The number of photons that are Raman scattered depends on the pathlength traversed by the photons. It is illustrative to look at the change in photon pathlength when for example clouds and aerosol are present in the atmosphere. An effective pathlength l_{eff} may be defined as (see Mayer et al., 1998, and references therein)

$$E_{\mathrm{abs}} = E_{\mathrm{no\,abs}} \exp(-\tau_{\mathrm{abs}} l_{\mathrm{eff}}/d) = E_{\mathrm{no\,abs}} \exp(-\tau_{\mathrm{abs}} \xi_{\mathrm{eff}}). \quad (6)$$

Here, the macroscopic effective pathlength enhancement, $\xi_{\mathrm{eff}} = l_{\mathrm{eff}}/d$, where d is the geometrical height of the cloud or aerosol layer. Furthermore, E_{abs} is the radiation

ACPD
10, 22515–22552, 2010

quantity of interest calculated with an additional absorber of small optical depth τ_{abs} while $E_{\text{no abs}}$ is the same quantity without the extra absorber.

2.1 Optically thick cloud/thunderstorm case

The thunderstorm took place over Garmisch-Partenkirchen on 19 June 1994, and has been described by Mayer et al. (1998). The sky was relatively cloudless in the morning. A large thunderstorm developed during the day with a maximum optical depth around 14:10 UTC. The cloudless, 07:46 UTC, and fully thunderstorm, 14:10 UTC, situations were simulated. Model input data were taken from Mayer et al. (1998, Table 1): for the fully developed thunderstorm at 14:10 UTC the solar zenith angle was 33°. The cloud was assumed to extend from 1 to 9 km with optical depth $\tau_{\text{wc}} = 340$. The effective droplet radius was set to 10.5 µm and the water cloud optical properties were calculated from the parameterization of Hu and Stamnes (1993). In addition sensitivity studies were made with optical properties from accurate Mie calculations based on Mie water cloud optical property tables available from http://www.libradtran.org.

For the cloudless case at 07:46 UTC the solar zenith angle was 57°. The wavelength dependent aerosol optical depth, τ_{aero}, was calculated using the Ångström formula, $\tau_{\text{aero}}=\beta\lambda^{-\alpha}$, with α=1.147 and β=0.20, as determined from direct sun measurements. The aerosol single scattering albedo was set to 0.95 and the aerosol asymmetry factor to 0.7. The aerosol was included in both the cloudy and cloudless situations. The consequences of excluding the aerosol for the thunderstorm situation are discussed by Mayer et al. (1998). For both situations a Lambertian surface albedo of 0.03 was assumed and the US midlatitude summer atmosphere was adopted (Anderson et al., 1986). The widely used ATLAS3 extraterrestrial spectrum was applied (Van-Hoosier, personal communication, 1996). The spectrum has been shifted from vacuum to air wavelengths using a formula provided by Teillet (1990).

ACPD
10, 22515–22552, 2010

2.2 Aerosol case

The modelled aerosol case was based on a situation that occurred during the actinic flux determination from measurements of irradiance (ADMIRA) measurement campaign, August 2000 at Nea Michaniona, Greece (Webb et al., 2002). Two spectra on 5 August were simulated. The first spectrum was measured at 11:20 UTC and the solar zenith angle varied from 25.69° at 340 nm to 25.82° at 410 nm. The Ångström coefficients were α=2.14 and β=0.038 giving $\tau_{aero}(\lambda$=400 nm)=0.27. The second spectrum was measured at 16:15 UTC and the solar zenith angle varied from 76.08° at 340 nm to 76.52° at 410 nm, with α=2.05 and β=0.027, giving $\tau_{aero}(\lambda$ = 400 nm)=0.18. The Lambertian surface albedo was set to vary linearly from 0.01 at 340 nm to 0.05 at 350 nm and 0.08 at 500 nm. The US standard atmosphere (Anderson et al., 1986) was used and the aerosol single scattering albedo and asymmetry factor taken from the rural spring-summer parameterisation of Shettle (1989). In this parameterisation the aerosol single scattering albedo and asymmetry factor vary with altitude and wavelength. The single scattering albedo takes on values between 0.94–0.98 while the asymmetry factor is about 0.67–0.70.

2.3 Sensitivity study cases

Several cloud and aerosol cases were considered for the sensitivity study. They are described in Sect. 4 together with the data analysis. Unlike the thunderstorm and aerosol cases, a single wavelength was chosen. The strong calcium H and K Fraunhofer absorption lines at 396.847 and 393.368 nm, respectively, give correspondingly large filling-in effects, see for example Figs. 1c and 2c. The sensitivity study calculations were done for 393.4 nm, at the center of the calcium K line.

Furthermore, bottom of the atmosphere (BOA), top of the atmosphere (TOA) and vertical profiles of filling-in factors were investigated. Filling-in factors were calculated both from irradiances and radiances, the latter including TOA nadir radiances applicable to satellite geometry and BOA zenith radiances applicable to ground-based measurement geometry.

ACPD
10, 22515–22552, 2010

3 Measurement comparisons

3.1 Thunderstorm case

The instrument setup for the thunderstorm case was described in detail by Mayer et al. (1998). The measurements were carried out in Garmisch-Partenkirchen, Germany (47.48° N, 11.07° E, and 730 m a.s.l.). The system for measuring spectral UV irradiance comprises a Bentham double monochromator DTM 300 with a photomultiplier as detector. Spectra of global irradiance were measured with a quartz cosine diffuser, and direct spectral irradiance was measured with narrow field-of-view entrance optics automatically aligned to the Sun. Calibrations were carried out on a weekly basis using 100 W tungsten-halogen standard lamps traceable to the Physikalisch Technische Bundesanstalt (PTB, Braunschweig, Germany). Spectra were recorded with a resolution of 0.6 nm and a step width of 0.25 nm between 285 and 410 nm. For the purpose of this study a very high wavelength alignment is required. Therefore the already very high wavelength accuracy (uncertainty typically 0.05 nm, carefully maintained by a spectral calculation with Mercury lamps) was further improved with the following procedure: the wavelength-dependent wavelength shift was determined by cross-correlation of the measured spectrum and a model calculation based on the same ATLAS3 spectrum used for all model calculations in this manuscript. The thus determined wavelength shift was added to each individual spectral point and finally the spectrum was interpolated to a regular 0.25 nm grid. The remaining wavelength uncertainty was in the order of 0.01–0.02 nm.

In Fig. 1a is shown the measured downwelling global (direct plus diffuse) irradiance at the surface for the cloudless (blue line) and thunderstorm (red line) cases. The thunderstorm cloud reduced the irradiance to about 2.5% of its cloudless value (Mayer et al., 1998). Also shown is the modelled cloudless irradiance (black line). The model/measurement ratio for the thunderstorm (red lines) and cloudless (blue lines) situations are shown in Fig. 1b. The model/measurement agreement is within the model and measurement uncertainties present in this spectral range, see e.g. Mayer et al.

ACPD
10, 22515–22552, 2010

(1997); Kylling et al. (1998); Van Weele et al. (2000); Hofzumahaus et al. (2002). Results for model calculations with (solid lines) and without (dotted lines) rotational Raman scattering are shown. The inclusion of rotational Raman scattering in the model calculations clearly improves the model/measurement ratio for both situations, and especially the thunderstorm situation.

The calculated FI for the thunderstorm situation is shown in Fig. 1c both at high-resolution and at the spectral resolution of the instrument. In this wavelength region rotational Raman scattering takes place within a wavelength interval of approximately ±2 nm. Thus, the spectral resolution of the instrument, about 0.6 nm, reduces the rotational Raman scattering signal by about 50% as is evident from Fig. 1c. Obviously the FI cannot be directly measured. For comparison of measured and modelled rotational Raman scattering effects the DOD is calculated. The cloudless spectrum is taken as E_{ref} and E is the thunderstorm spectrum. The DODs calculated from the measured and calculated spectra are shown in Fig. 1d. There is generally good agreement between the measured and calculated DODs. Differences are seen at around 360, 380, and 400 nm. The cause of these differences is not known, but the data suggests that it is due to measurement uncertainties.

At the time of Mayer et al. (1998) it was quite common to use the Henyey-Greenstein phase function, e.g. as in the parameterization by Hu and Stamnes (1993), to describe cloud optical properties for irradiance calculations. For radiance calculations the difference between a Heyney-Greenstein phase function and exact Mie calculations may of course be substantial. To investigate the effects on irradiances, the simulations were repeated with phase functions from exact Mie theory calculations (the so-called Mie tables available from http://www.libradtran.org). The cloud droplet sizes were assumed to be described by a gamma-distribution with α=7 and the effective radius r_{eff}=10 µm. For more details see Emde et al. (2010, Sect. 2.3). The resulting DOD is shown in green in Fig. 1d. Using the exact phase function reduces the DOD by up to 25% for the investigated case. There are two reasons for this. The effective pathlength of the photons may be calculated as explained in Sect. 4. For photons that travel through the cloud, the

ACPD
10, 22515–22552, 2010

pathlength increases by about 2% when changing from the Heyney-Greenstein phase function to the Mie phase function. As absorbing aerosols are also present in the cloud, this increase in pathlength leads to increased absorption of photons and hence less Raman scattering. By excluding aerosols there is still a difference in the DODs calculated using either the Heyney-Greenstein phase function or the Mie phase function, with a smaller DOD for the Mie phase function. It is estimated that for the present case the aerosol accounts for about two thirds of the reduction in the DOD. The remaining difference is caused by differences in the phase functions. The Mie phase function has a larger back-scattering part, see for example Mayer and Kylling (2005, Fig. 6), thus less photons make it through the cloud. This implies that less photons are available for scattering into the wavelength of interest compared to a Heyney-Greenstein phase function. Hence, the DOD is further reduced for the Mie phase function.

3.2 Aerosol case

The spectra for the aerosol case were measured with a Bentham DTM300 double monochromator spectroradiometer (Blumthaler et al., 2008). For these measurements the instrument was equipped with gratings with 2400 lines per mm, resulting in a slit width of 0.48 nm (FWHM). The spectra were recorded with a step size of 0.25 nm.

The spectral calibration is routinely checked against the structure of the Fraunhofer lines, which results in an overall absolute uncertainty of the spectral alignment of less than 0.1 nm. The precision of the spectral alignment is better than 0.05 nm. For further improvement of the spectral alignment, the spectra were corrected using the ShicRIVM algorithm Slaper et al. (1995), which yields a reproducibility of the wavelength setting of the spectra on the level of 0.01 nm.

The absolute calibration is based on a 1000 W halogen lamp, traceable to the Physikalisch Technische Bundesanstalt (PTB, Braunschweig, Germany). The integration time when reading out the photomultiplier current is adapted to the absolute level of the signal in order to achieve a good signal to noise ratio at each wavelength. For wavelengths above 340 nm this is usually 20 ms, which leads to a statistical noise in

ACPD
10, 22515–22552, 2010

the order of 0.3%. The overall spectral noise, when comparing two consecutive spectra in the wavelength range between 340 nm and 410 nm is in the order of 0.5%.

The measured and simulated aerosol spectra are shown in Fig. 2a. The model/measurement ratios are shown in Fig. 2b and the agreement between model and measurement is similar to that shown in Fig. 1b for the thunderstorm case. The filling-in factor for the 16:15 UTC spectrum is shown in Fig. 2c. The filling-in is about a factor 2.5 less than for the thunderstorm case. The measured and modelled DODs for the aerosol case are shown in Fig. 2d. As for the thunderstorm case there is very good agreement between the measured and modelled DODs. The effect of rotational Raman scattering is significantly smaller for the aerosol case than for the thunderstorm case. This is so even if in the thunderstorm case the direct optical path increases by a factor of 1.54 when the solar zenith angle increases from 33° to 57°, while for the aerosol case the pathlength increases by 3.71 when the solar zenith angle increases from 26° to 76°. The larger differential optical depth for the thunderstorm case is caused by multiple scattering within the cloud which increases the photon path length and thus the likelihood of a Raman scattering event.

4 Sensitivity studies

4.1 Solar zenith angle

To investigate the sensitivity of FI factors to the solar zenith angle under cloudy conditions, FI factors were calculated for TOA and BOA radiances and irradiances as a function of the solar zenith angle. The calculations were made for a cloud of optical depth 10 with cloud bottom at 1 km and vertical thickness of 1 km. The cloud single scattering albedo and asymmetry factor were calculated using the Hu and Stamnes (1993) parameterization with an effective droplet radius of 10.5 µm as above. The surface at 0 km had a Lambertian surface albedo of 0.03. The calculated BOA irradiance (dotted red line) and zenith radiance (solid red line) FI factors in Fig. 3, have similar behaviour as

ACPD
10, 22515–22552, 2010

a function of solar zenith angle. The TOA irradiance FI factor (dotted blue line) varies little for solar zenith angles below about 55° after which it increases. The TOA nadir radiance FI factor (solid blue line) has a similar behaviour with solar zenith angle as the BOA quantities, except the maximum in the FI is at a smaller solar zenith angle, 85°, compared to 88° for the BOA quantities. The increase in FI with solar zenith angle is caused by the increase in the diffuse versus global radiation as the solar zenith angle increases. As the solar zenith angle increases further the likelihood of a single scattering event before the photon reaches the cloud increases. Thus for very large solar zenith angles the photons will travel in a more direct way to the BOA or TOA, hence the decrease in the filling-in factors at these angles. It it noted that the TOA results have similar behaviour to those presented by Joiner et al. (1995, Figs. 8 and 9).

4.2 Cloud optical depth

The variation of FI with cloud optical depth is shown in Fig. 4 for a solar zenith angle of 33°. The cloud geometry and optical properties are similar to those used for Fig. 3, except that the cloud optical depth is varied from 0 to 500. It is noted that a cloud optical depth of 500 is unrealistic for a cloud with a 1 km extension. The calculations for such large optical depths may nevertheless be instructive. The nadir radiance and irradiance based FI-factors starts levelling off at optical depths larger then about 50 and reaches values of about 8.4 and 10.07%, respectively for a cloud optical depth τ_{wc}=500. The radiance results are consistent with similar results from de Beek et al. (2001) and Lambert Equivalent Reflectivity (LER) results from Joiner and Bhartia (1995). The BOA zenith FI-factors show no sign of levelling off. When the cloud optical thickness increases the cloud more and more resembles a semi-infinite scattering medium. Thus, the pathlength increase of photons backscattered into the upper hemisphere will level off and the FI behave correspondingly. Below the cloud, the photon path length will increase as long as the cloud optical depth increases. A larger photon path length increases the chance for a Raman scattering event. Hence, the FI-factors increase with increased cloud optical depth for surface based zenith-viewing instruments. Obviously,

ACPD
10, 22515–22552, 2010

the absolute zenith radiance and irradiance are rather small for optically very thick clouds.

4.3 Cloud vertical extent

The calculations for Figs. 3 and 4 were performed with a cloud extending from 1 to 2 km. To test the sensitivity of the FI-factor to the vertical cloud extent, the cloud bottom was fixed at 1 km and the cloud top height varied from 2 to 15 km. This was done for cloud optical depths of 10, 50, 100, 200 and 500. The resulting FI-factors calculated from TOA nadir radiances are shown in Fig. 5. FI-factors calculated from BOA zenith radiances and irradiances, not shown, are minimally influenced by the cloud top height. Also shown in Fig. 5 is the filling-in when using the so-called Lambert Equivalent Reflectivity (LER) model. In this model the clouds are treated as a reflecting surface at a specific pressure level. Thus radiation transport in the cloud is not considered implying that path length increases in the cloud are not accounted for. The LER concept has been used to derive cloud top pressure Joiner and Bhartia (1995). The Modified LER (MLER) model tries to remedy the neglect of photon transport within the cloud by setting the cloud reflectivity to some large value and mixing clear and cloudy scene radiation fields (Ahmad et al., 2004). The LER and MLER model are applicable for satellite geometries. Here, the LER filling-in was calculated for a surface albedo of 0.65 (Joiner et al., 2004). The pressure of the surface was decreased from 1013 to 121 mb. The LER model does not account for path length effects due to scattering in the cloud (Ahmad et al., 2004). It therefore underestimates the filling-in as shown in Fig. 5.

4.4 Filling-in vertical profiles and clouds

Similar to the model of Spurr et al. (2008), the present model may calculate the radiation field anywhere in the atmosphere. In Fig. 6 vertical profiles of the filling-in factor are shown for the same cloud as in Spurr et al. (2008, Fig. 8). The cloud layer was between

ACPD
10, 22515–22552, 2010

2 and 3 km, with a single scattering albedo of 0.9999 and a Heyney-Greenstein phase function with asymmetry factor 0.8. The solar zenith angle was set to 45°. Filling-in factor profiles are shown for cloud optical depths of 0.1, 1.0, 2.0 and 10.0 as calculated from both radiances (upper row Fig. 6) and irradiances (lower row Fig. 6). The results for the diffuse downward and upward filling-in irradiance factors, solid lines in the lower row Fig. 6, agree reasonably well with those presented by Spurr et al. (2008, Fig. 8). Differences may be attributed to the different solution methods employed for the solution of the Raman scattering source term; Spurr et al. (2008) use a Green's function method while the present work employs standard discrete ordinate methods (Stamnes et al., 1988; Kylling and Stamnes, 1992). Concerning the downwelling radiation it is clear that the cloud has little impact on the filling-in factor calculated from the global irradiance (dashed lines, lower row, left plot Fig. 6). Hence, measurement of this quantity will hardly give any cloud information. The filling-in factors calculated from the upward irradiance clearly exhibit the signature of the cloud. For the global downwelling radiation the radiation field above the cloud is dominated by the direct beam, hence the filling-in is small. In and below the cloud the radiation field becomes diffuse and the global filling-in approaches the diffuse filling-in for clouds of optical thickness greater than 1. For the upwelling irradiance filling-in factor the clouds decrease the filling-in above the cloud. This is caused by a decrease in the photon path length due to the presence of the cloud.

The behaviour of the filling-in factors calculated from the zenith and nadir radiances, upper row Fig. 6, are rather different from those calculated from the irradiances, lower row Fig. 6. The zenith filling-in factor profile develops a distinct minimum at 2.7 km, within the cloud. The nadir filling-in factor profile develops a distinct maximum at 2.1 km. To understand these results it is instructive to look at the radiance in the principal plane at various altitudes below, inside and above the cloud. In Fig. 7 is shown the radiances calculated with and without Raman scattering at the bottom of the atmosphere, 1.9, 2.1, 2.3, 2.5, 2.7, 2.9, 3.1 km, and top of the atmosphere. The angular distribution of diffuse radiation changes dramatically with altitude and especially within the cloud. At the

ACPD
10, 22515–22552, 2010

top of the atmosphere, upper left plot Fig. 7, there is no downwelling diffuse radiation and the upwelling diffuse radiation is fairly homogeneous. Just above the cloud top, at 3.1 km, a majority of the diffuse radiation is in the upward direction, but some radiation is also scattered downwards by the above atmosphere. The diffuse radiation field is asymmetric due to the chosen solar zenith angle of 45°. Once inside the cloud the picture changes dramatically. The strongly forward scattering water droplets gives a strong lobe in the direction of the direct sun ray. As one moves deeper into the cloud the lobe broadens due to multiple scattering. But still at the bottom of the cloud there is an asymmetry in the radiance field. Thus, within a cloud of optical depth 10, there should be little problem to distinguish up from down based on the diffuse radiation field. Due to the low surface albedo (0.05), there is little diffuse upwelling radiation below the cloud. At the bottom of the atmosphere there is still some asymmetry in the radiation field. This asymmetry is large enough to be measurable.

From the radiances with and without Raman scattering included, filling-in factors may be calculated as shown in Fig. 8. The angular behaviour of the filling-in reflects the path length travelled by the individual photons. In the direction of the direct sun ray near the top of the cloud some photons have been scattered once and thus the chance of a Raman scattering event is small. For the other directions the photons have increasingly been scattered several times and hence the chance of a Raman event increases. This is seen in the correspondingly large filling-in factors in the upper hemisphere within the cloud. The filling-in varies considerably with viewing angle and the minima at 2.5, 2.7 and 2.9 km, in the direction of the direct sun ray stand out in particular. Results are shown for one solar zenith angle. Clearly, the picture will be different for other solar zenith angles and cloud situations. Specifically, within the upper part of the cloud the radiance calculated filling-in will vary with solar zenith angle.

4.5 Plane-parallel versus pseudo-spherical geometry

Ground-based measurement of trace gases using zenith radiance measurements are often done for large solar zenith angles for which the sphericity of the Earth's

ACPD
10, 22515–22552, 2010

atmosphere may be of importance. In Fig. 9 is shown FI factors calculated from BOA zenith radiances. The calculations were made both in pseudo-spherical and plane-parallel geometry for a cloudless atmosphere with no aerosol and aerosol optical depths of 0.12 and 0.42. For solar zenith angles smaller than about 77° the difference between the plane-parallel and the pseudo-spherical calculations is less than 1%. The overestimation of the FI by plane-parallel geometry then increases with increasing solar zenith angle. As the plane-parallel geometry overestimates the photon path length for large solar zenith angles, too many Raman scattering events will be included. The overestimation is not very sensitive to the aerosol load. Clearly, pseudo-spherical geometry is needed for trace gas retrievals at large solar zenith angles.

4.6 Aerosol effects on surface radiances

MAX-DOAS, see Wittrock et al. (2004); Wagner et al. (2009b) and references therein, techniques utilize the measurement of radiances in off-axis (non-zenith) directions to derive trace gas concentrations and aerosol information. As such, off-axis FI-factors are of interest. As an example of the effect of aerosols on FI-factors BOA radiances were calculated with and without Raman scattering. The upper row in Fig. 10 shows the radiance at 393.4 nm for aerosol optical depths of 0.0, 0.12 and 0.42. The location of the sun is easily seen in the middle plot for an aerosol optical depth of 0.12. For Rayleigh and Raman scattering only, upper left plot, the nearly isotropic Rayleigh and Raman scattering phase functions make variations in the radiance field small with azimuth angle. There is a distinct minimum in the zenith direction for all three aerosol optical depths as this is the direction where the photon path length is smallest. The forward peaked aerosol scattering phase function gives the radiance maximum in the sun's direction in the middle upper plot. For such small aerosol optical depths single scattering dominates. For larger optical depths multiple scattering increase thus reducing the variations in the radiance, upper right plot. The corresponding FI-factors are shown in the lower row of Fig. 10. The FI-factors exhibit an opposite behaviour of the radiance as the FI-factors are largest in the zenith direction and close to the horizon

ACPD
10, 22515–22552, 2010

and smallest in the direction of the sun and 180° away from the sun. This is due to the forward scattering nature of the aerosol particles. The forward peaked phase function leads to a shorter path length for the photons thus decreasing the FI-factor. This effect decreases with increasing optical depth which gives more multiple scattering. Thus the variation in the FI is smaller for τ_{aero}=0.42 than for τ_{aero}=0.12. The filling-in in general decreases with increased aerosol optical depth in agreement with the findings of Langford et al. (2007) and Wagner et al. (2009b).

5 Conclusions

A new radiative transfer model including single rotational Raman scattering has been presented. Differential optical depths calculated with the model agree well with measurements for both thunderstorm and aerosol loaded cases. Thus, inclusion of rotational Raman scattering in the model simulations explains the spectral structures seen in the measured differential optical depths.

Several sensitivity studies have been made to investigate effects of clouds and aerosols on filling-in of Fraunhofer lines due to rotational Raman scattering. These studies confirm results from other studies including:

- The TOA filling-in increases with increasing solar zenith angle, exhibiting a maximum at around 85° before it decreases.
- Filling-in factors calculated from TOA irradiances and zenith radiances levels off for cloud optical depths larger than about 50.
- The so-called Lambert Equivalent Reflectivity (LER) model underestimates filling-in due to lack of photon transport within the clouds.
- The filling-in factor profiles calculated from irradiances throughout a cloud, exhibit the same vertical structure as seen by Spurr et al. (2008).

ACPD
10, 22515–22552, 2010

In addition it was found that

- Filling-in factors calculated from BOA irradiances and nadir radiances increases with increasing cloud optical depth due to the increase in photon path lengths.
- For cloudy cases the choice of phase function, Heyney-Greenstein or exact phase function from Mie theory, may significantly affect the calculated effects of rotational Raman scattering.
- Filling-in profiles from zenith and nadir radiances within clouds have a distinctly different behaviour than filling-in factors from irradiances.
- Polar plots of radiances and filling-in factors from radiances exhibits strong asymmetries deep inside and below clouds.
- For solar zenith larger than about 77° the plane-parallel geometry overestimates the filling-in compared to the the pseudo-spherical approximation.
- The filling-in at the bottom of the atmosphere varies between 8 and 16% depending on viewing angle and aerosol optical depth for the atmospheric situation studied here.

The radiative transfer model, including rotational Raman scattering, is available from http://www.libradtran.org.

Appendix A

The solution method

The solution of Eq. (1) starts with the splitting of the global radiation field in a direct and a diffuse component. Furthermore, rotational Raman scattering is a small effect and is treated as a perturbation (Vountas et al., 1998). Multiple rotational Raman scattering

ACPD
10, 22515–22552, 2010

gives subpercentage contributions to the total radiation field (van Deelen et al., 2007). Thus, only first order rotational Raman scattering is included below. By expanding the radiance in a Fourier cosine series, $I(\tau,\pm\mu,\Phi)=\sum_{m=0}^{2N-1} I_m(\tau,\pm\mu)\cos m(\Phi_0-\Phi)$, writing the phase function in terms of Legendre polynomials, applying the addition theorem for spherical harmonics and replacing the integral over μ in Eq. (1) with a sum using double Gaussian quadrature, the discrete ordinate version of Eq. (1) is obtained (Chandrasekhar, 1960; Stamnes et al., 1988; Spurr et al., 2008):

$$\begin{aligned}\mu_i \frac{dI^m(\tau_\lambda,\mu_i)}{d\tau_\lambda} &= I^m(\tau_\lambda,\mu_i) \\ &\quad -\frac{\omega_\lambda^{\mathrm{E}}(\tau_\lambda)}{2}\sum_{\substack{j=-1\\ j\neq 0}}^{j=1} c_j \Pi_d^{\mathrm{E}}(\tau_{\lambda_s},\mu_i,\mu_j) I^m(\tau_\lambda,\mu_j) \\ &\quad -\frac{\omega_\lambda^{\mathrm{E}}(\tau_\lambda) I_\lambda^0}{4\pi}(2-\delta_{0,m})\Pi_b^{\mathrm{E}}(\tau_{\lambda_s},\mu_i,\mu_0) e^{-T(\tau_\lambda)} \\ &\quad -Q^m(\tau_\lambda,\mu_i), \end{aligned} \tag{A1}$$

$$\begin{aligned}Q^m(\tau_\lambda,\mu_i) &= +\sum_{s=1}^{\mathrm{NS}} \frac{\omega_{\lambda_s}^R(\tau_{\lambda_s})}{2}\sum_{\substack{j=-1\\ j\neq 0}}^{j=1} c_j \Pi_d^R(\tau_{\lambda_s},\mu_i,\mu_j) I^{E,m}(\tau_{\lambda_s},\mu_j) \\ &\quad +\sum_{s=1}^{\mathrm{NS}} \frac{\omega_{\lambda_s}^R(\tau_{\lambda_s}) I_{\lambda_s}^0}{4\pi}(2-\delta_{0,m})\Pi_b^R(\tau_{\lambda_s},\mu_i,\mu_0) e^{-T(\tau_{\lambda_s})} \\ &\quad -\frac{\omega_\lambda^{\mathrm{RL}}(\tau_\lambda)}{2}\sum_{\substack{j=-1\\ j\neq 0}}^{j=1} c_j \Pi_d^R(\tau_\lambda,\mu_i,\mu_j) I^{E,m}(\tau_\lambda,\mu_j) \end{aligned}$$

ACPD
10, 22515–22552, 2010

$$-\frac{\omega_\lambda^{\mathrm{RL}}(\tau_\lambda) I_\lambda^0}{4\pi}(2-\delta_{0,m})\Pi_b^R(\tau_\lambda,\mu_i,\mu_0)e^{-T(\tau_\lambda)}, \tag{A2}$$

Here μ_i and c_i are quadrature angles and weights, respectively. The three different single scattering albedos for the elastic, Raman gain and Raman loss scattering terms, are calculated according to Stamnes (1986); Spurr et al. (2008) as:

$$\omega_\lambda^{\mathrm{E}}(\tau_\lambda) = \frac{\beta^{\mathrm{sca}}(z,\lambda)}{\beta^{\mathrm{ext}}(z,\lambda)} \tag{A3}$$

$$\omega_\lambda^{\mathrm{R}}(\tau_{\lambda_\mathrm{s}}) = \frac{\rho_{\mathrm{air}}(z)\left(\zeta_{\mathrm{O}_2}\sigma_{\mathrm{O}_2}^{\mathrm{RRS}}(\lambda_\mathrm{s},\lambda)+\zeta_{\mathrm{N}_2}\sigma_{\mathrm{N}_2}^{\mathrm{RRS}}(\lambda_\mathrm{s},\lambda)\right)}{\beta^{\mathrm{ext}}(z,\lambda)} \tag{A4}$$

$$\omega_\lambda^{\mathrm{RL}}(\tau_\lambda) = \frac{\rho_{\mathrm{air}}(z)\left(\zeta_{\mathrm{O}_2}\sum_{s=1}^{\mathrm{NS}_{\mathrm{O}_2}}\sigma_{\mathrm{O}_2}^{\mathrm{RRS}}(\lambda,\lambda_\mathrm{s})+\zeta_{\mathrm{N}_2}\sum_{s=1}^{\mathrm{NS}_{\mathrm{N}_2}}\sigma_{\mathrm{N}_2}^{\mathrm{RRS}}(\lambda,\lambda_\mathrm{s})\right)}{\beta^{\mathrm{ext}}(z,\lambda)} \tag{A5}$$

The relative abundances of O_2 and N_2 are set to ζ_{O_2}=0.2095 and ζ_{N_2}=0.7905. The elastic single scattering albedo $\omega_\lambda^{\mathrm{E}}$ is the same as used in the elastic calculation. The rotational Raman scattering cross section is denoted by σ^{RRS} and $\rho_{\mathrm{air}}(z)$ is the density of air. The phase function is expanded in associated Legendre polynomials $\Lambda_l^m(\mu)$ as

$$\Pi_b^{x,m}(\tau,\mu,\mu') = \sum_{l=m}^{2M-1}(2l+1)g_l^x(\tau)(-1)^{l+m}\Lambda_l^m(\mu)\Lambda_l^m(\mu_0) \tag{A6}$$

$$\Pi_d^{x,m}(\tau,\mu,\mu') = \sum_{l=m}^{2M-1}(2l+1)g_l^x(\tau_{\lambda_\mathrm{s}})\Lambda_l^m(\mu)\Lambda_l^m(\mu'), \tag{A7}$$

where x=E (Elastic), R (Raman). The Raman phase function $P^{\mathrm{R}}(\Phi)=\frac{3}{40}(13+\cos^2\Phi)$ so for x=R only terms for m=0,1,2 contribute in the above sums. The transmission

ACPD
10, 22515–22552, 2010

$T(\tau)$ is calculated in pseudo-spherical geometry to account for the sphericity of the Earth's atmosphere (Dahlback and Stamnes, 1991). Finally τ_s is the optical depth at wavelength s.

Equations (A1)–(A2) are a system of $2N$ coupled differential equations for which analytic solutions do not exist. To obtain analytic solutions, it is assumed that the atmosphere consists of L adjacent layers where the single scattering albedo and the phase function are assumed to be constant. The analytic solutions for each layer are coupled by requiring the intensity to be continuous across layer interfaces, see Stamnes et al. (1988) for details. Finally, the following boundary conditions at the top and bottom of the atmosphere are applied:

$$I(\tau, -\mu, \Phi) = I_{\text{top}}(\mu, \Phi) \tag{A8}$$

$$I(\tau = \tau_L, +\mu, \Phi) = I_g(\mu, \Phi) \tag{A9}$$

where $I_{\text{top}}(\mu, \Phi)$ is diffuse downwelling radiation at the top of the atmosphere (usually zero) and $I_g(\mu, \Phi)$ is upwelling radiation at the bottom of the atmosphere $\tau=\tau_L$ (usually represented by a surface albedo A).

A solution of an equation similar to Eq. (A1), but with a general source term instead of direct beam source term and the Raman scattering source terms, has been given by Kylling and Stamnes (1992). The qdisort solver included in libRadtran (Mayer and Kylling, 2005, www.libradtran.org), is an implementation of this solution procedure. In addition to the particular solution for the general source term it also includes particular solutions for the direct beam source and optionally a thermal source. The solution of the transport equation for a general source term is given in Kylling and Stamnes (1992) and will not be repeated here.

The solution of Eq. (1) as implemented in libRadtran thus includes first order rotational Raman scattering and absorption and multiple elastic scattering of molecules, aerosols and clouds. A total of 233 Raman lines, NS_{O_2}=185 for O_2 and NS_{N_2}=48 for N_2, are considered following Chance and Spurr (1997) and de Haan et al. (2003).

ACPD
10, 22515–22552, 2010

Acknowledgements. Model development was supported by the ESA-funded project ESASLight, ESTEC contract AO/1-5433/07/NL/HE.

References

Ahmad, Z., Bhartia, P. K., and Krotkov, N.: Spectral properties of backscattered UV radiation in cloudy atmospheres, J. Geophys. Res., 109, D01201, doi:10.1029/2003JD003395, 2004. 22528

Anderson, G., Clough, S., Kneizys, F., Chetwynd, J., and Shettle, E.: AFGL atmospheric constituent profiles (0–120 km), Tech. Rep. AFGL-TR-86-0110, Air Force Geophys. Lab., Hanscom Air Force Base, Bedford, Mass., 1986. 22521, 22522

Blumthaler, M., Schallhart, B., Schwarzmann, M., McKenzie, R., Johnston, P., Kotkamp, M., and Shiona, H.: Spectral UV measurements of global irradiance, solar radiance, and actinic flux in New Zealand: intercomparison between instruments and model calculations, J. Atm. Ocean Technol., 25(6), 945–958, 2008. 22525

Chance, K. and Spurr, R. J. D.: Ring effect studies: Rayleigh scattering including molecular parameters for rotational Raman scattering, and the Fraunhofer spectrum, Appl. Opt., 36, 5224–5230, 1997. 22536

Chandrasekhar, S.: Radiative Transfer, Dover, Mineola, NY, 1960. 22534

Dahlback, A. and Stamnes, K.: A new spherical model for computing the radiation field available for photolysis and heating at twilight, Planet. Space Sci., 39, 671–683, 1991. 22536

de Beek, R., Vountas, M., Rozanov, V. V., Richter, A., and Burrows, J.: The ring effect in the cloudy atmospheres, Geophys. Res. Lett., 28, 721–724, 2001. 22517, 22520, 22527

de Haan, J. F., Veefkind, J. P., van Oss, R., Levelt, P. F., and Noordhoek, R.: Accounting for Raman scattering in DOAS, Tech. Rep., SN-OMIE-KNMI-409, 2003. 22536

Emde, C., Buras, R., Mayer, B., and Blumthaler, M.: The impact of aerosols on polarized sky radiance: model development, validation, and applications, Atmos. Chem. Phys., 10, 383–396, doi:10.5194/acp-10-383-2010, 2010. 22517, 22524

Hofzumahaus, A., Kraus, A., Kylling, A., and Zerefos, C.: Solar actinic radiation (280–420 nm) in the cloud-free troposphere between ground and 12 km altitude: measurements and model results, J. Geophys. Res., 107, 8139, doi:10.1029/2001JD900142, 2002. 22524

Hu, Y. X. and Stamnes, K.: An accurate parameterization of the radiative properties of water

ACPD

10, 22515–22552, 2010

clouds suitable for use in climate models, J. Climate, 6, 728–742, 1993. 22521, 22524, 22526
Joiner, J. and Bhartia, P. K.: The determination of cloud pressure from rotational Raman scattering in satellite backscatter ultraviolet measurements, J. Geophys. Res., 100, 23019–23026, 1995. 22520, 22527, 22528
Joiner, J., Bhartia, P. K., Cebula, R. P., Hilsenrath, E., McPeters, R. D., and Park, H.: Rotational Raman scattering (ring effect) in satellite backscatter ultraviolet measurements, Appl. Opt., 21, 4513–4525, 1995. 22517, 22527
Joiner, J., Vasilkov, A. P., Flittner, D. E., Gleason, J. F., and Bhartia, P. K.: Retrieval of cloud pressure and oceanic chlorophyll content using Raman scattering in GOME ultraviolet spectra, J. Geophys. Res., 109, D01109, doi:10.1029/2003JD003698, 2004. 22528
Kattawar, G. W., Young, A. T., and Humphreys, T. J.: Inelastic scattering in planetary atmospheres. I. The ring effect, without aerosols, Astrophys. J., 243, 1049–1057, 1981. 22516
Kylling, A. and Stamnes, K.: Efficient yet accurate solution of the linear transport equation in the presence of internal sources: the exponential-linear-in-depth approximation, J. Comput. Phys., 102, 265–276, 1992. 22529, 22536
Kylling, A., Bais, A. F., Blumthaler, M., Schreder, J., Zerefos, C. S., and Kosmidis, E.: Effect of aerosols on solar UV irradiances during the photochemical activity and solar ultraviolet radiation campaign, J. Geophys. Res., 103, 26051–26060, 1998. 22524
Kylling, A., Webb, A. R., Bais, A. F., Blumthaler, M., Scmitt, R., Thiel, S., Kazantzidis, A., Kift, R., Misslbeck, M., Schallhart, B., Schreder, J., Topaloglou, C., Kazadzis, S., and Rimmer, J.: Actinic flux determination from measurements of irradiance, J. Geophys. Res., 108, 4506, doi:10.1029/2002JD003236, 2003. 22519
Landgraf, J., Hasekamp, O. P., van Deelen, R., and Aben, I.: Rotational Raman scattering of polarized light in the Earth atmosphere: a vector radiative transfer model using the radiative transfer perturbation theory approach, J. Quant. Spectrosc. Ra., 87, 399–433, 2004. 22517, 22518
Langford, A. O., Schofield, R., Daniel, J. S., Portmann, R. W., Melamed, M. L., Miller, H. L., Dutton, E. G., and Solomon, S.: On the variability of the Ring effect in the near ultraviolet: understanding the role of aerosols and multiple scattering, Atmos. Chem. Phys., 7, 575–586, doi:10.5194/acp-7-575-2007, 2007. 22520, 22532
Mayer, B. and Kylling, A.: Technical note: The libRadtran software package for radiative transfer calculations – description and examples of use, Atmos. Chem. Phys., 5, 1855–1877,

ACPD
10, 22515–22552, 2010

doi:10.5194/acp-5-1855-2005, 2005. 22516, 22519, 22525, 22536
Mayer, B., Seckmeyer, G., and Kylling, A.: Systematic long-term comparison of spectral UV measurements and UVSPEC modeling results, J. Geophys. Res., 102, 8755–8767, 1997. 22523
Mayer, B., Kylling, A., Madronich, S., and Seckmeyer, G.: Enhanced absorption of UV radiation due to multiple scattering in clouds: experimental evidence and theoretical explanation, J. Geophys. Res., 103, 31241–31254, 1998. 22519, 22520, 22521, 22523, 22524
Shettle, E. P.: Models of aerosols, clouds and precipitation for atmospheric propagation studies, paper presented at Conference on Atmospheric Propagation in the UV, Visible, IR and MM-Region and Related System Aspects, NATO Adv. Group for Aerosp. Res. and Dev., Copenhagen, 1989. 22522
Slaper, H., Reinen, H. A. J. M., Blumthaler, M., Huber, M., and Kuik, F.: Comparing ground-level spectrally resolved solar UV measurements using various instruments: a technique resolving effects of wavelengths shift and slit width, Geophys. Res. Lett., 22, 2721–2724, 1995. 22525
Spurr, R., de Haan, J. D., van Oss, R., and Vasilkov, A.: Discrete ordinate radiative transfer in a stratified medium with first order rotational Raman scattering, J. Quant. Spectrosc. Ra., 109, 404–425, 2008. 22517, 22520, 22528, 22529, 22532, 22534, 22535, 22548
Stamnes, K.: The theory of multiple scattering of radiation in plane parallel atmospheres, Rev. Geophys., 24, 299–310, 1986. 22518, 22535
Stamnes, K., Tsay, S.-C., Wiscombe, W., and Jayaweera, K.: Numerically stable algorithm for discrete-ordinate-method radiative transfer in multiple scattering and emitting layered media, Appl. Opt., 27, 2502–2509, 1988. 22516, 22529, 22534, 22536
Teillet, P. M.: Rayleigh optical depth comparisons from various sources, Appl. Opt., 29, 1897–1900, 1990. 22521
van Deelen, R., Hasekamp, O. P., and Landgraf, J.: Accurate modeling of spectral fine-structure in Earth radiance spectra measured with the global ozone monitoring experiment, Appl. Opt., 46, 243–252, 2007. 22517, 22534
Van Weele, M., Martin, T. J., Blumthaler, M., Brogniez, C., den Onter, P. N., Engelsen, O., Lenoble, J., Mayer, B., Pfister, G., Ruggaber, A., Walravens, B., Weihs, P., Gardiner, P. G., Gillotay, D., Haferl, D., Kylling, A., Seckmeyer, G., and Wauben, W. M. F.: From model intercomparison towards benchmark UV spectra for six real atmospheric cases, J. Geophys. Res., 105, 4916–4925, 2000. 22524
Vountas, M., Rozanov, V. V., and Burrows, J. P.: Ring effect: impact of rotational Raman scat-

ACPD
10, 22515–22552, 2010

tering on radiative transfer in Earht's atmosphere, J. Quant. Spectrosc. Ra., 60, 943–961, 1998. 22517, 22518, 22533

Wagner, T., Beirle, S., and Deutschmann, T.: Three-dimensional simulation of the ring effect in observations of scattered sun light using Monte Carlo radiative transfer models, Atmos. Meas. Tech., 2, 113–124, doi:10.5194/amt-2-113-2009, 2009a. 22517

Wagner, T., Deutschmann, T., and Platt, U.: Determination of aerosol properties from MAX-DOAS observations of the ring effect, Atmos. Meas. Tech., 2, 495–512, doi:10.5194/amt-2-495-2009, 2009b. 22517, 22531, 22532

Wagner, T., Beirle, S., Deutschmann, T., and de Vries, M. P.: Determination of aerosol properties from satellite observations of the ring effect, Atmos. Meas. Tech. Discuss., 3, 3535–3599, doi:10.5194/amtd-3-3535-2010, 2010. 22517

Webb, A. R., Bais, A. F., Blumthaler, M., Gobbi, G.-P., Kylling, A., Schmitt, R., Thiel, S., Barnaba, F., Danielsen, T., Junkermann, W., Kazantzidis, A., Kelly, P., Kift, R., Liberti, G. L., Misslbeck, M., Schallhart, B., Schreder, J., and Topaloglou, C.: Measuring spectral actinic flux and irradiance: experimental results from the ADMIRA (Actinic Flux Determination from Measurements of Irradiance), J. Atm. Ocean Technol., 19, 1049–1062, 2002. 22522

Wittrock, F., Oetjen, H., Richter, A., Fietkau, S., Medeke, T., Rozanov, A., and Burrows, J. P.: MAX-DOAS measurements of atmospheric trace gases in Ny-Ålesund – radiative transfer studies and their application, Atmos. Chem. Phys., 4, 955–966, doi:10.5194/acp-4-955-2004, 2004. 22531

ACPD

10, 22515–22552, 2010

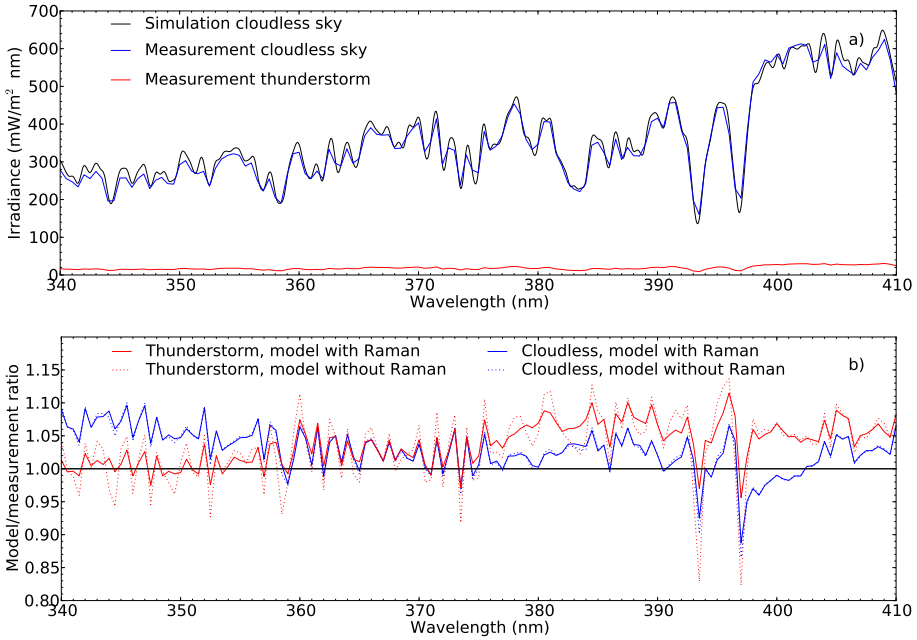

Fig. 1. (a) The measured (red and blue lines) and simulated (black line) spectra under cloudless (blue) and thunderstorm (red) situations. **(b)** The model/measurement ratio for the cloudless and thunderstorm situations. Ratios are shown for model simulations with and without rotational Raman scattering. **(c)** The filling-in factor for the thunderstorm situation as calculated from simulated spectra at high spectral resolution and at instrument resolution. **(d)** The measured and simulated DOD. Simulations with both a Heyney-Greenstein phase function (blue) and an exact Mie phase function (green) are shown.

ACPD
10, 22515–22552, 2010

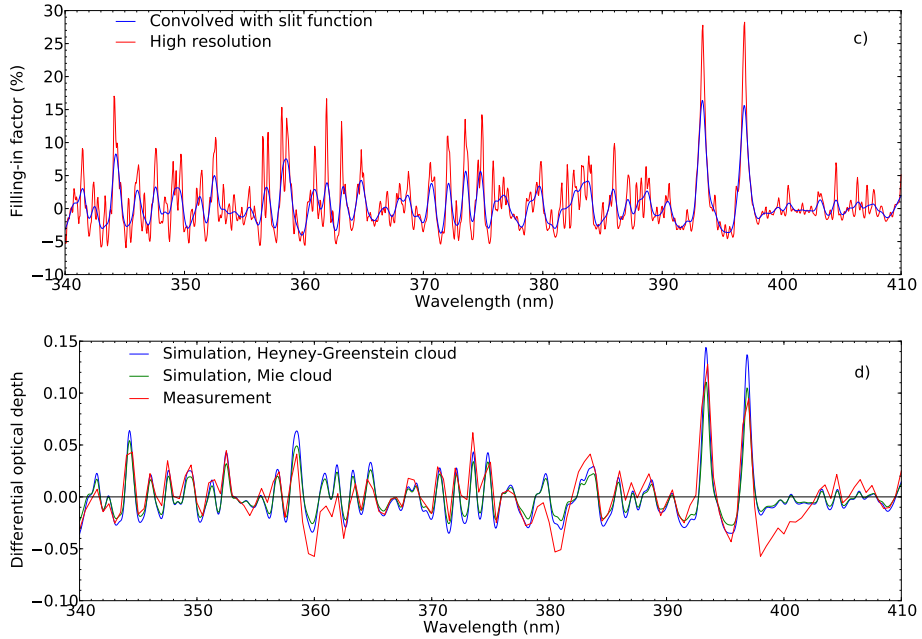

Fig. 1. Continued.

ACPD
10, 22515–22552, 2010

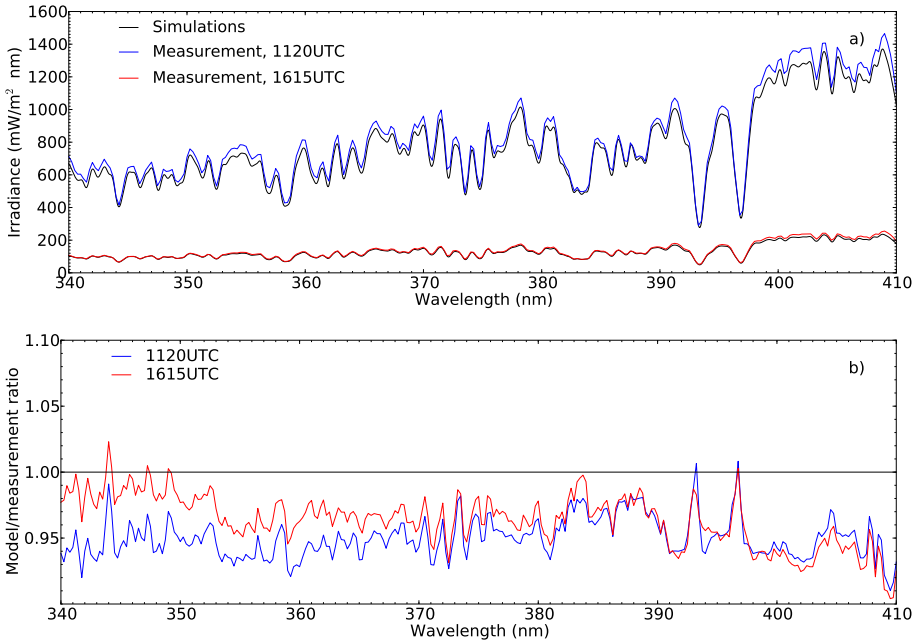

Fig. 2. (a) The measured spectra at 11:20 UTC (blue line) and 16:15 UTC (red line). The corresponding model simulations are shown black. **(b)** Model/measurement ratios for the 12:10 UTC (blue line) and 16:15 UTC (red line) spectra. **(c)** The filling-in factor for the 16:15 UTC spectrum as calculated from simulated spectra at high spectral resolution and at instrument resolution. **(d)** The measured (red line) and simulated (blue line) DODs. Note difference in *y*-axis scale from Fig. 1d.

ACPD
10, 22515–22552, 2010

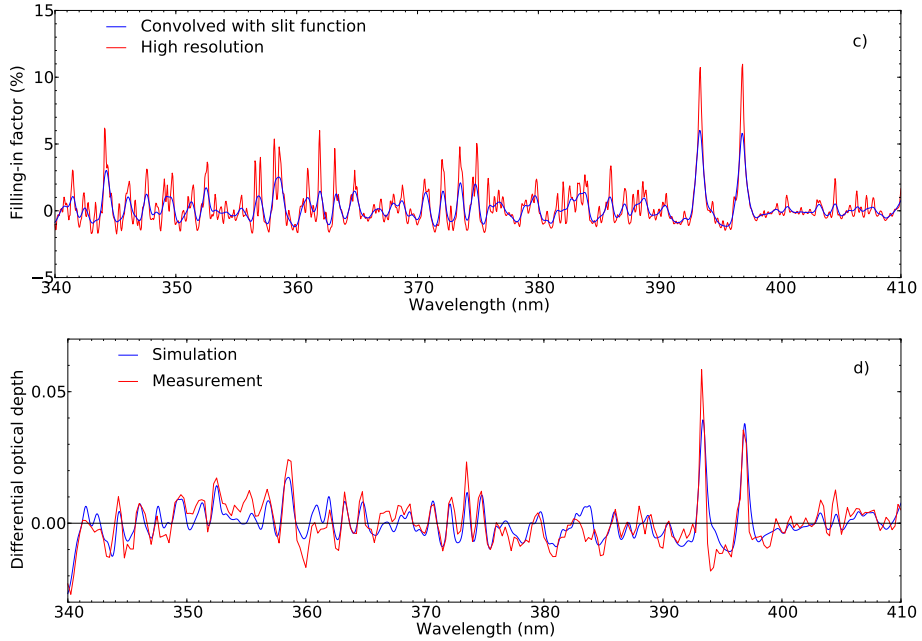

Fig. 2. Continued.

ACPD
10, 22515–22552, 2010

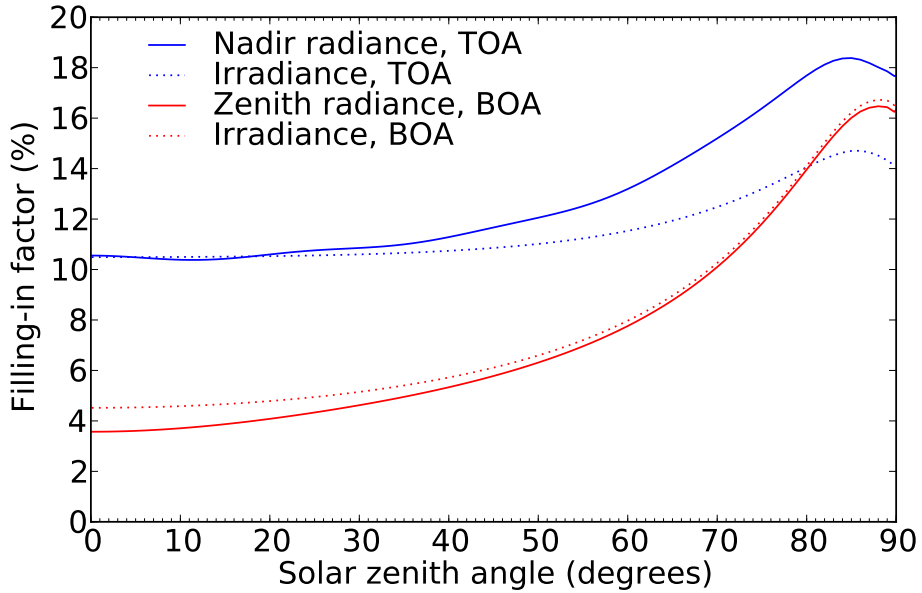

Fig. 3. The filling-in factor at 393.4 nm as a function of solar zenith angle for a cloud of optical depth 10. Cloud bottom is at 1 km and cloud top at 2 km with the surface at 0.0 km. Top of the atmosphere (TOA) and bottom of the atmosphere (BOA) FI factors calculated from radiances and irradiances are shown.

ACPD
10, 22515–22552, 2010

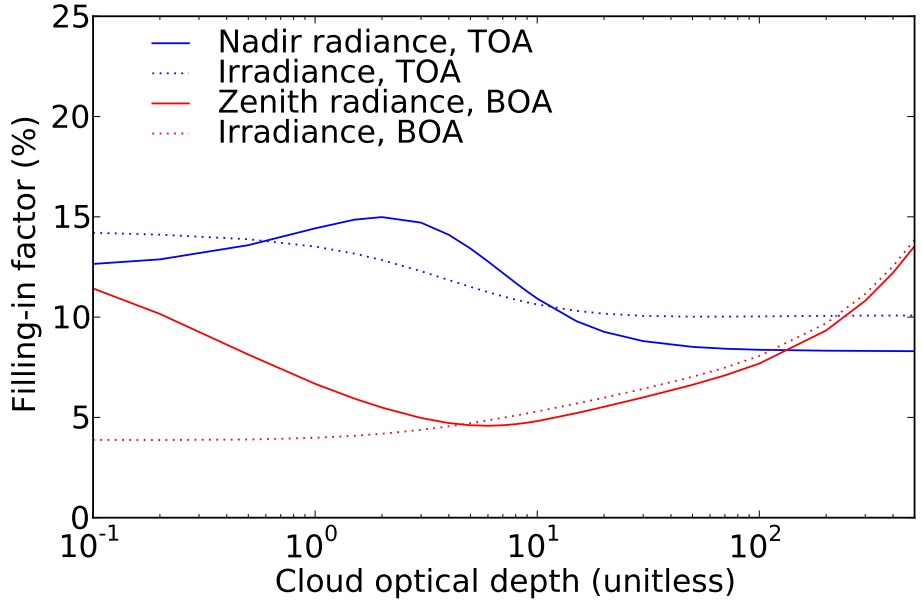

Fig. 4. The filling-in factor at 393.4 nm as a function of cloud optical depth. Cloud bottom is at 1 km and cloud top at 2 km with the surface at 0.0 km. Top of the atmosphere (TOA) and bottom of the atmosphere (BOA) FI factors calculated from radiances and irradiances are shown.

ACPD
10, 22515–22552, 2010

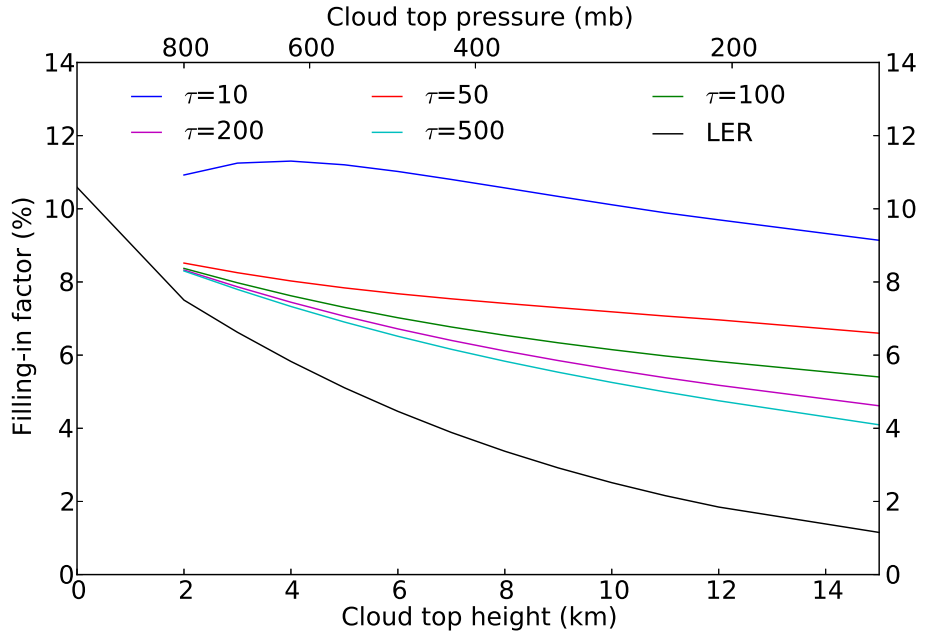

Fig. 5. The filling-in factor at 393.4 nm as a function of cloud top height. Cloud bottom is at 1 km with the surface at 0.0 km. Top of the atmosphere (TOA) FI factors as calculated from nadir radiances are shown for various cloud optical depths and for a Lambert reflecting surface with varying surface pressure (upper x-axis).

ACPD
10, 22515–22552, 2010

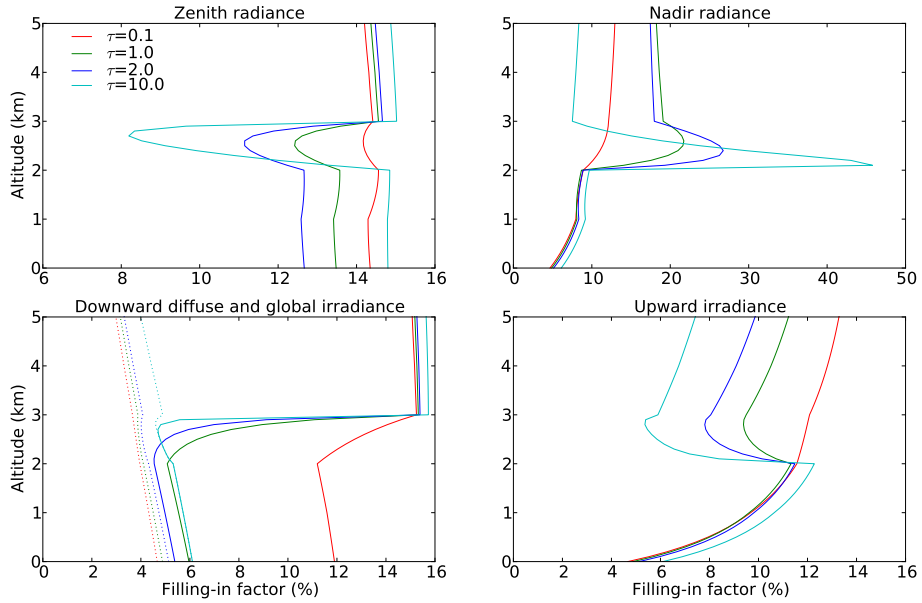

Fig. 6. Profiles of the filling-in factor as calculated from radiances (top row) and irradiances (bottom row). Solid lines represents filling-in factors calculated from radiances (upper row) and diffuse upward and downward irradiances (lower row). Dashed lines are filling-in factors calculated from the global (direct plus diffuse downward) irradiance. As in Spurr et al. (2008) the cloud layer was located between 2 and 3 km and the surface at 0.0 km. Note differences in the scales of the *x*-axes.

ACPD
10, 22515–22552, 2010

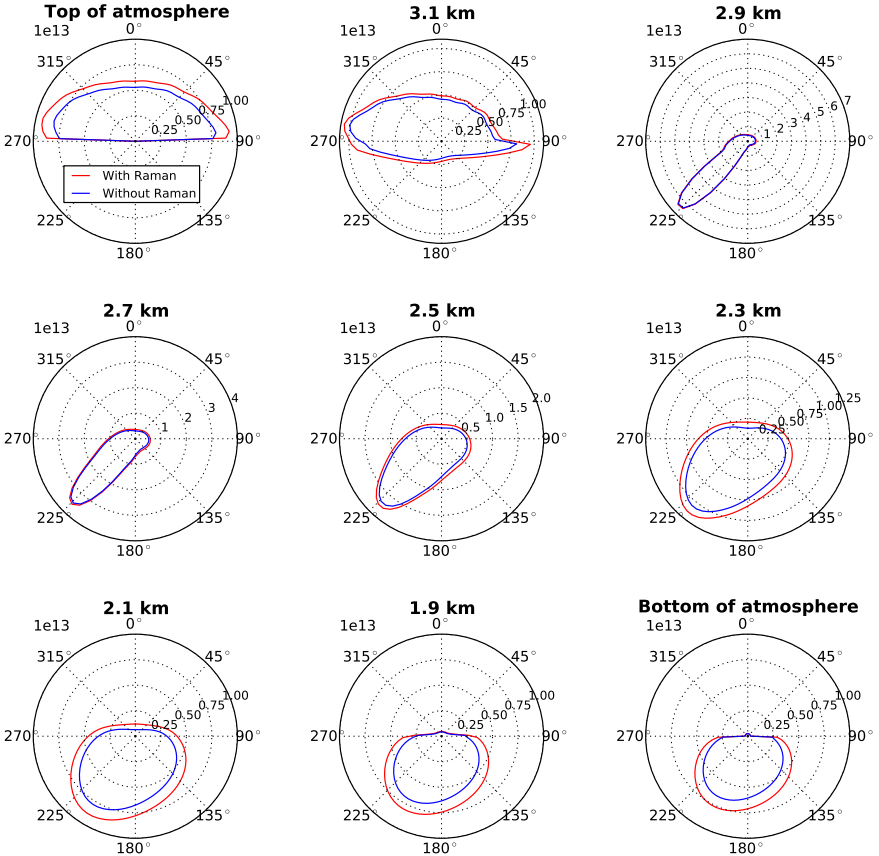

Fig. 7. The radiance [photons/(s cm^2 nm sr)] in the principal plane for various altitudes. The polar angle gives the direction of the radiation. A polar angle of 0° gives radiation travelling in the zenith direction. The sun is incident at 45°. The atmospheric conditions are as in Fig. 6 with a cloud of optical depth of 10 located between 1 and 2 km. Note that the scales on the various plots differ.

ACPD
10, 22515–22552, 2010

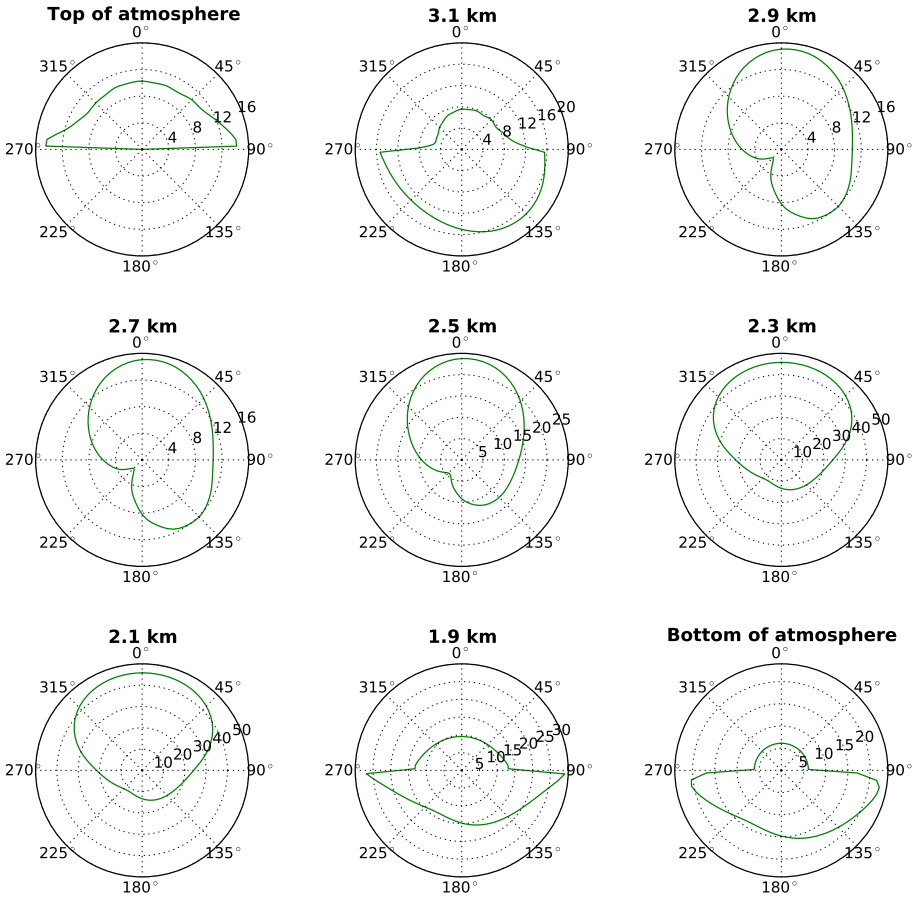

Fig. 8. The filling-in factor (%) in the principal plane for various altitudes. The polar angle gives the direction of the radiation. Calculated from the radiances in Fig. 7. Note that the scales on the various plots differ.

ACPD
10, 22515–22552, 2010

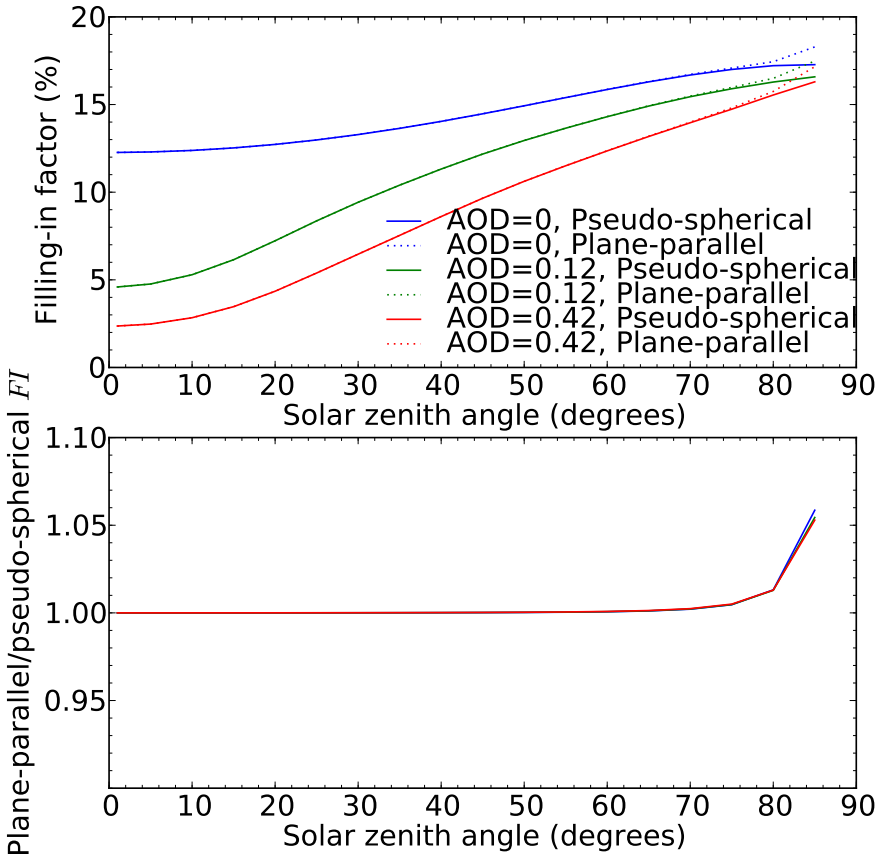

Fig. 9. Upper plot: The zenith filling-in factor at 393.4 nm as a function of solar zenith angle for various aerosol optical depths. Filling-in factors are calculated using both pseudo-spherical (solid lines) and plane-parallel (dotted lines) geometry. Lower plot: The ratio of FI factors calculated in plane-parallel and pseudo-spherical geometry.

ACPD
10, 22515–22552, 2010

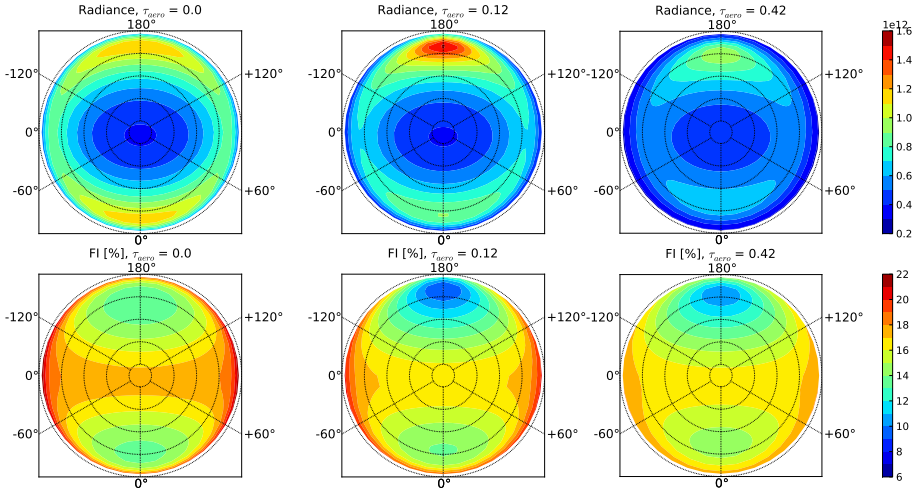

Fig. 10. The upper row shows the BOA radiance [photon/(s cm^2 nm sr)] at 393.4 nm for various aerosol optical depths for a solar zenith angle of 85°. The azimuth angle varies between ±180° and the dotted circles indicate polar angles of 10, 30, 50, 70, and 90° moving outwards. The lower row shows corresponding FI-factors.

ACPD
10, 22515–22552, 2010